Building-block-flow model for LES of high-speed flows

By R. Ma†, Y. Yuan†, G. Arranz†, Y. Ling†, R. Agrawal, M. P. Whitmore, A. Elnahhas, C. Pederson‡ AND A. Lozano-Durán†¶

A wall model for large-eddy simulation (LES) is developed accounting for compressibility and roughness effects in high-speed regimes. The model is implemented using machine learning (ML) techniques and trained with a new direct numerical simulation (DNS) database of compressible turbulent flow over rough walls for various wall roughness topographies, Mach numbers, and Reynolds numbers. Information-theoretic dimensionless learning is employed to determine the nondimensional inputs and outputs for the wall model with the highest predictive power. The performance of the wall model is assessed *a-posteriori* in compressible turbulent channel flows with both smooth and rough walls, a high-speed compression ramp with roughness, and an entry, descent, and landing (EDL)-like vehicle with roughness. The results demonstrate that the new wall model can predict drag and heat flux for high-speed flows in hydraulically smooth, transitionally rough, and fully rough regimes with a typical accuracy ranging from 1% to 12%.

1. Introduction

Computational fluid dynamics (CFD) for EDL vehicles faces unique challenges due to the complexity of the aerodynamics and thermodynamics involved (Hollis *et al.* 2014). Some of the challenges include roughness-enhanced heat transfer and skin friction of ablated thermal protection systems (TPS), flow separation behind blunt bodies, strong shock waves, high-enthalpy effects, and laminar-to-turbulent transition (Dirling 1973; Finson & Clarke 1980; Bowersox 2007; Gaitonde & Adler 2023). Hollis (2014) has highlighted the deficiency of current CFD closure models for predicting multiple aerothermodynamic phenomena, particularly those involving strong compressibility effects and roughness-enhanced heating and shearing.

Wall-modeled large-eddy simulation (WMLES) has emerged as a useful computational technique for modeling the effects of the small-scale flow and surface geometries on the outer flow, rather than resolving the near-wall region directly. It leads to substantial cost savings over wall-resolved LES, which makes calculations of high-speed engineering applications tractable. Recent works demonstrate the predictive capability of WMLES for high-speed flows (Kawai & Larsson 2010; Yang *et al.* 2018; Iyer & Malik 2019; Mettu & Subbareddy 2022; Griffin *et al.* 2023). However, the current wall models are mostly limited by the degraded performance in flows with strong compressibility effects and complex geometries. Moreover, existing wall models fail to account for the impact of surface roughness in amplifying shear forces and heat transfer in high-speed flows.

In this report, we address these limitations by developing a wall model for LES that models compressibility and surface roughness effects. The approach, referred to as the

† Department of Aeronautics and Astronautics, Massachusetts Institute of Technology
‡ NASA Langley Research Center
¶ Graduate Aerospace Laboratories, California Institute of Technology

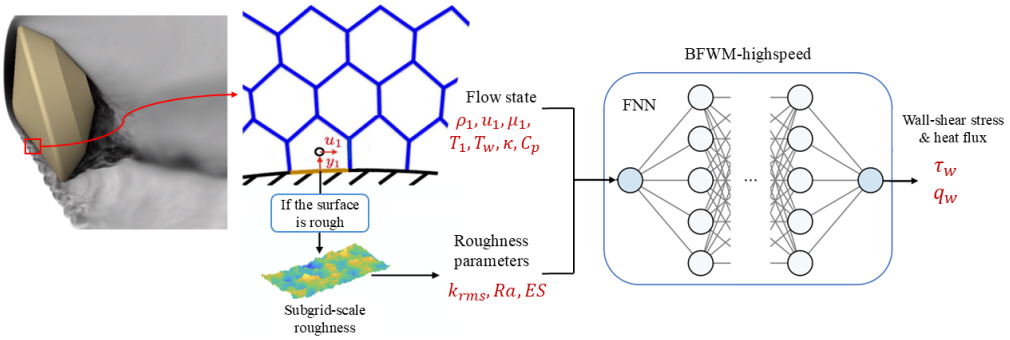

FIGURE 1. Overview of the BFWM-highspeed: using flow state at the wall and the first control volume off the wall and roughness statistical parameters as the inputs to the wall model, and the wall-shear stress and heat flux are the outputs. A feedforward neural network (FNN) is used to construct the wall model.

building-block-flow wall model for high-speed flows (BFWM-highspeed), builds upon our prior experience with low-speed flows over smooth and rough walls (Lozano-Durán & Bae 2023; Arranz *et al.* 2024; Ma & Lozano-Durán 2024). Our focus is on aerospace applications, such as blunt-body EDL vehicles at high speed in the presence of rough surfaces, though the model is generally applicable to other engineering scenarios.

The report is organized as follows. An overview of the model, training data preparation, simulation setup, and the method of dimensionless learning are provided in Section 2. Results for *a-posteriori* testing of WMLES in turbulent channel flows, a compression ramp, and an EDL vehicle are presented in Section 3. Finally, concluding remarks are summarized in Section 4.

2. Methodology

2.1. *Model overview*

The main assumption of the BFWM is that a collection of simple canonical flows contains the key physics necessary to predict the wall-shear stress and heat flux in more complex flow scenarios. This approach was introduced by Lozano-Durán & Bae (2023) for low-speed flows. An overview of the BFWM-highspeed is shown in Figure 1.

The model uses flow information at the wall and at the first control volume off the wall y_1 as inputs. This includes the density ρ_1, wall-parallel velocity u_1, temperature T_1, wall temperature T_w, dynamic viscosity μ_1, thermal conductivity κ, and specific heat capacity c_p of the flow. The model operates in two modes: smooth wall (BFWM-smooth) and rough wall (BFWM-rough). In the latter, the mean geometric properties of the surface roughness are also provided as inputs. These include the root-mean-square roughness height k_{rms}, the first-order roughness height fluctuations R_a, and the effective slope ES. The definitions of these roughness parameters are given by Ma & Lozano-Durán (2024). These three parameters are considered to sufficiently represent the geometrical features of Gaussian roughness (Ma *et al.* 2021). To ensure the generalization of the wall model, the input features are nondimensional combinations of the variables described above. Information-theoretic dimensionless learning is used to discover the most informative dimensionless input features, and this is discussed in Section 2.3.

The DNS and WMLES presented here are conducted with an explicit, unstructured,

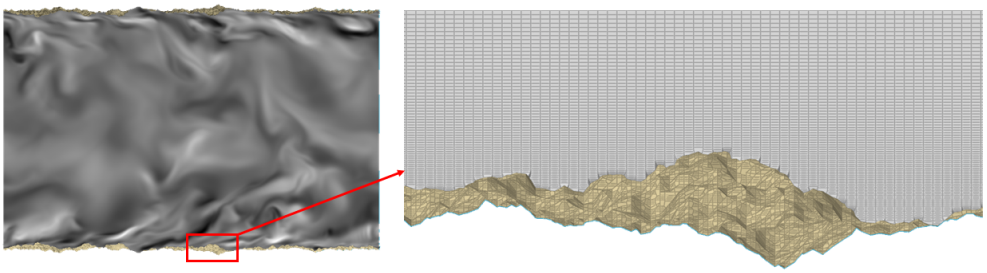

FIGURE 2. Instantaneous streamwise velocity for DNS of a minimal-span channel flow over a rough wall. The zoom-in view shows the grid in the near-wall region. The wetted rough surfaces are colored in dark yellow.

finite-volume solver, charLES, which solves compressible Navier-Stokes equations (Fu *et al.* 2021). The meshes are generated based on the Voronoi tessellation. The Vreman subgrid-scale model (Vreman 2004) is used for *a-posteriori* testing of BFWM-highspeed in WMLES.

2.2. *Training database*

The training database comprises new DNS of turbulent channel flows over smooth and rough surfaces. We generated 15 irregular, multiscaled rough surfaces by prescribing the probability density function of a Gaussian distribution and the power spectra of isotropic self-affine fractals (Pérez-Ràfols & Almqvist 2019). The naming convention we used for these 15 rough surfaces is RS#, and the range of their key roughness parameters are $k_{rms}/R_a = 1.17 \sim 1.33$ and $ES = 0.12 \sim 0.71$. The simulations are driven with uniform volumetric momentum and energy source terms to achieve $M_c = \frac{U_c}{\sqrt{\gamma R T_w}} = 0.5, 1, 2, 4$ and $Re_c = \frac{\rho_c U_c \delta}{\mu_w} = 4000, 8000, 16000$, where ρ_c and U_c are the mean density and velocity at the channel centerline, respectively; T_w and μ_w are the mean temperature and dynamic viscosity at the wall, respectively; and δ is the channel half-height. The mean is referred to the average in all homogeneous directions (i.e., streamwise, spanwise) and time. The values of M_c and Re_c were chosen to cover both transitionally and fully rough regimes, as well as typical flow conditions in high-speed flow applications (Hollis 2014). As a result, the present DNS database comprises a total of 180 rough cases and 12 smooth cases. The simulation details of the reference cases are summarized in Table 1.

A minimal-span channel simulation approach is used (MacDonald *et al.* 2017) to alleviate the computational cost of generating the DNS database. This is justified as only mean flow data in the near-wall region are required to train the wall model. A preliminary comparison between the minimal- and full-span smooth channel flows showed that errors for the mean velocity and temperature profiles are within 2% at $y = 0.1\delta$. As such, the wall model was trained using DNS mean flow data within $0 < y \leq 0.1\delta$. The domain size is $L_x = 3\delta$, $L_y = 2\delta$, and $L_z = \delta$, following the criteria proposed by MacDonald *et al.* (2017). A visualization of the flow field and meshes in the near-wall region is shown in Figure 2. Uniform grids are used in the streamwise and spanwise directions, while stretched grids based on a hyperbolic tangent function are used in the wall-normal direction.

Case	M_c	Re_c	M_b	Re_τ	Re_τ^*	$-B_q$	Δx^+	Δy^+_{min}	$\Delta y_{max}/\delta$	Δz^+
Mc0.5Rec4000	0.5	4000	0.43	278	267	0.004	2.1	0.04	0.009	1.7
Mc0.5Rec8000	0.5	8000	0.43	496	478	0.004	3.7	0.07	0.009	3.0
Mc0.5Rec16000	0.5	16000	0.43	921	889	0.004	6.9	0.13	0.009	5.6
Mc1.0Rec4000	1.0	4000	0.85	288	251	0.016	2.2	0.04	0.009	1.8
Mc1.0Rec8000	1.0	8000	0.86	523	456	0.015	4.0	0.08	0.009	3.2
Mc1.0Rec16000	1.0	16000	0.87	960	842	0.014	7.3	0.14	0.009	5.9
Mc2.0Rec4000	2.0	4000	1.69	328	202	0.06	2.5	0.05	0.009	2.0
Mc2.0Rec8000	2.0	8000	1.71	597	370	0.05	4.5	0.09	0.009	3.7
Mc2.0Rec16000	2.0	16000	1.72	1068	685	0.05	8.1	0.15	0.009	6.5
Mc4.0Rec4000	4.0	4000	3.25	450	117	0.19	3.4	0.06	0.009	2.7
Mc4.0Rec8000	4.0	8000	3.39	772	229	0.16	5.8	0.11	0.009	4.7
Mc4.0Rec16000	4.0	16000	3.44	1320	421	0.16	10.0	0.19	0.009	8.1

TABLE 1. Simulation details of the reference smooth cases in the DNS database. The friction Reynolds number $Re_\tau = \rho_w u_\tau \delta/\mu_w$, where $u_\tau = \sqrt{\tau_w/\rho_w}$, and the transformed friction Reynolds number is $Re_\tau^* = \rho_c\sqrt{\tau_w/\rho_c}\delta/\mu_c$ (Coleman *et al.* 1995), where the subscript c denotes the mean flow quantity at the channel centerline. The wall heat transfer rate is $B_q = q_w/(\rho_w c_p u_\tau T_w)$. The + denotes the viscous unit based on u_τ and ν_w, where ν_w is the kinematic viscosity at the wall.

2.3. *Information-theoretic dimensionless learning*

We introduce an information-theoretic, data-driven dimensionless learning method that identifies the best-performing dimensionless inputs to predict the nondimensional quantity of interest. Consider the vector of dimensional input variables $\mathbf{q} = [q_1, q_2, \ldots, q_n]$, and the dimensional output q_o. The goal is to discover p nondimensional inputs, denoted by $\mathbf{\Pi} = [\Pi_1, \ldots, \Pi_p]$, that provide the highest predictive capabilities of the nondimensional output Π_o. The method consists of two steps:

Step 1: First, the Buckingham-Π theorem is used to construct dimensionless candidates $\mathbf{\Pi}$. The i-th dimensionless number has the form $\Pi_i = \prod_{j=1}^n q_j^{a_{ij}} = \mathbf{q}^{\mathbf{a}_i}$, where $\mathbf{a}_i = [a_{i1}, a_{i2}, \ldots, a_{in}]^T$ is the vector of exponents for Π. The input candidate $\mathbf{\Pi}$ is then obtained from the solution to $\boldsymbol{D}\mathbf{a}_i = 0$, where $\boldsymbol{D}$ is the dimension matrix containing the powers of the fundamental units for $\mathbf{q}$, $\boldsymbol{D} = [\boldsymbol{d}_1, \boldsymbol{d}_2, \ldots, \boldsymbol{d}_n]$, and $\boldsymbol{d}_i$ is the dimensional vector for the physical quantity q_i. For example, the velocity $q_1 = u = [\text{length}]^1[\text{mass}]^0[\text{time}]^{-1}[\text{temperature}]^0$ has $\boldsymbol{d}_1 = [1, 0, -1, 0]$ and so on. The solution $\mathbf{a}_i$ can be expressed as $\mathbf{a}_i = \sum_{j=1}^{n-k} c_{ij}\mathbf{w}_j = \mathbf{W}\mathbf{c}_i$, where $\boldsymbol{W} = [\boldsymbol{w}_1, \boldsymbol{w}_2, \ldots, \boldsymbol{w}_{n-k}]$ is the matrix of basis vectors of the null space of $\boldsymbol{D}$, and $\mathbf{c}_i = \left[c_{i1}, c_{i2}, \ldots, c_{i(n-k)}\right]$ is the coefficient vector corresponding to $\boldsymbol{w}_i$. In conclusion, nondimensional inputs are obtained by $\mathbf{\Pi(C)} = \mathbf{q}^{\mathbf{WC}} = \left[\mathbf{q}^{\mathbf{Wc}_1}, \mathbf{q}^{\mathbf{Wc}_2}, \ldots, \mathbf{q}^{\mathbf{Wc}_p}\right]$, where the constant in $\mathbf{C} = [\mathbf{c}_1, \mathbf{c}_2, \ldots, \mathbf{c}_p]$ can be chosen arbitrarily.

Step 2: An infinite number of nondimensional inputs exist; however, not all are useful for predicting the nondimensional output. Here, we identify the dimensionless input with the highest predictive capabilities. Let us denote by $\epsilon\left(\mathbf{\Pi}, \hat{f}\right) = \left\|\Pi_o - \hat{\Pi}_o\right\|_2$ the error of a model $\hat{f}$ aiming to predict Π_o using the inputs $\mathbf{\Pi}$, i.e., $\hat{\Pi}_o = \hat{f}(\mathbf{\Pi})$. It can be shown that the minimum error across all possible models $\hat{f}$ is bounded by,

$$\epsilon_{\min}\left(\mathbf{\Pi}\right) = \min_{\hat{f}} \epsilon\left(\mathbf{\Pi}, \hat{f}\right) \geq \frac{1}{\sqrt{2e\pi}} e^{h(\Pi_o) - I(\Pi_o; \mathbf{\Pi})}, \tag{2.1}$$

where $h(\Pi_o)$ is the differential entropy of Π_o, and $I\left(\Pi_o; \mathbf{\Pi}\right)$ is the mutual information measuring the information shared between Π_o and $\mathbf{\Pi}$ (Cover 1999). The mutual infor-

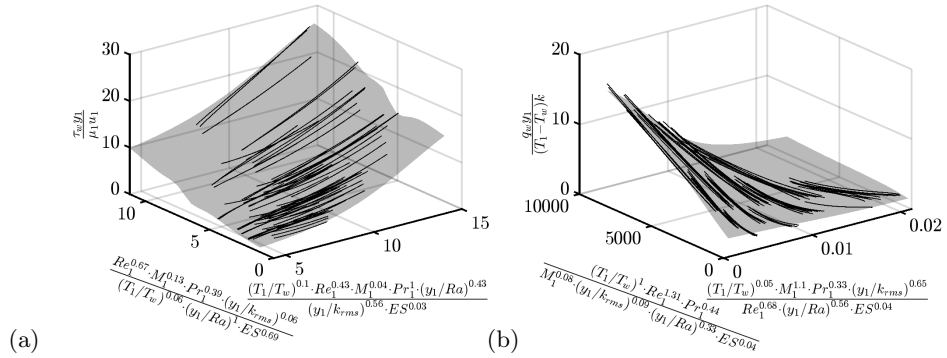

FIGURE 3. The dimensionless (a) wall-shear stress and (b) wall heat flux as a function of the optimized dimensionless inputs. The lines represent DNS mean flow data of different cases for $y < 0.1\delta$. The surface corresponds to the prediction from the neural network wall model.

mation is $I\left(\Pi_o; \mathbf{\Pi}\right) = \int \rho_{\Pi,\Pi_o}\left(\boldsymbol{\pi}, \pi_o\right) \log\left(\frac{\rho_{\Pi,\Pi_o}(\boldsymbol{\pi},\pi_o)}{\rho_\Pi(\boldsymbol{\pi})\rho_{\Pi_o}(\pi_o)}\right) \mathrm{d}\boldsymbol{\pi}\mathrm{d}\pi_o$, where ρ_{Π,Π_o} is the joint probability distribution of $\mathbf{\Pi}$ and Π_o, and ρ_Π and ρ_{Π_o} are the marginal probabilities of $\mathbf{\Pi}$ and Π_o, respectively. For a given Π_o, the value of $h(\Pi_o)$ is fixed and the nondimensional input with the best predictive capabilities is that maximizing $I\left(\Pi_o; \mathbf{\Pi}\right)$,

$$\mathbf{\Pi}(\mathbf{C}) = \arg\max_{\mathbf{\Pi}} I\left(\Pi_o; \mathbf{\Pi}(\mathbf{C})\right) = \arg\max_{\mathbf{C}} I\left(\Pi_o; \mathbf{\Pi}(\mathbf{C})\right). \tag{2.2}$$

The optimization problem can be effectively solved using the covariance matrix adaptation evolution strategy (CMA-ES) introduced by Hansen *et al.* (2003).

The dimensionless forms of the outputs are $\frac{\tau_w y_1}{\mu_1 u_1}$ for the wall-shear stress and $\frac{q_w y_1}{\kappa(T_1 - T_w)}$ for the wall heat flux. The input variables are $\mathbf{q} = [y_1, u_1, \rho_1, T_1, T_w, \mu_1, k, c_p, k_{rms}, R_a, ES]^T$. Here, we show the results for BFWM-rough. The results for BFWM-smooth are omitted for brevity. For both wall-shear stress and heat flux, the number of inputs is set to $p = 2$, as it was found that increasing the number of inputs beyond this provides only marginal improvements in the maximization of the mutual information $I\left(\Pi_o; \mathbf{\Pi}\right)$. The CMA-ES algorithm is run with a population size of 50, lower and upper bounds for c_{ij} set to $[-2, 2]$, and a maximum of 50,000 iterations. The algorithm was initialized with a standard deviation of 0.5. The optimal dimensionless inputs discovered for predicting wall-shear stress are

$$\mathbf{\Pi}_{\tau_w} = \arg\max_{\mathbf{\Pi}} I\left(\frac{\tau_w y_1}{\mu_1 u_1}; \mathbf{\Pi}\right) = \left[\frac{\left(\frac{T_1}{T_w}\right)^{0.1} \cdot Re_1^{0.43} \cdot M_1^{0.04} \cdot Pr_1^1 \cdot \left(\frac{y_1}{Ra}\right)^{0.43}}{\left(\frac{y_1}{k_{rms}}\right)^{0.56} \cdot ES^{0.03}}, \frac{Re_1^{0.67} \cdot M_1^{0.13} \cdot Pr_1^{0.39} \cdot \left(\frac{y_1}{k_{rms}}\right)^{0.06}}{\left(\frac{T_1}{T_w}\right)^{0.06} \cdot \left(\frac{y_1}{Ra}\right)^1 \cdot ES^{0.69}}\right],$$

and the optimal dimensionless inputs discovered for predicting wall heat flux are

$$\mathbf{\Pi}_{q_w} = \arg\max_{\mathbf{\Pi}} I\left(\frac{q_w y_1}{\kappa(T_1 - T_w)}; \mathbf{\Pi}\right) = \left[\frac{\left(\frac{T_1}{T_w}\right)^{0.05} \cdot M_1^{1.1} \cdot Pr_1^{0.33} \cdot \left(\frac{y_1}{k_{rms}}\right)^{0.65}}{Re_1^{0.68} \cdot \left(\frac{y_1}{Ra}\right)^{0.56} \cdot ES^{0.04}}, \frac{\left(\frac{T_1}{T_w}\right)^1 \cdot Re_1^{1.31} \cdot Pr_1^{0.44}}{M_1^{0.08} \cdot \left(\frac{y_1}{k_{rms}}\right)^{0.09} \cdot \left(\frac{y_1}{Ra}\right)^{0.33} \cdot ES^{0.04}}\right],$$

where M_1, Pr_1, and Re_1 is the local Mach, Prandtl, and Reynolds number at the first grid point off the wall. Using the identified optimal dimensionless inputs, we train two

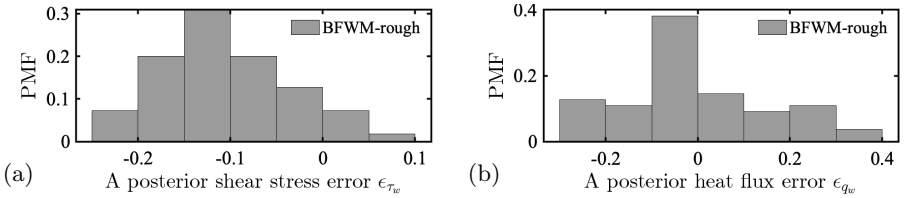

FIGURE 4. The probability mass function (PMF) of *a-posteriori* error for (a) the wall-shear stress and (b) the wall heat flux of WMLES using BFWM-highspeed over all 180 cases. The *a-posteriori* error in wall-shear stress, ϵ_{τ_w}, is defined as $\epsilon_{\tau_w} = \frac{\hat{\tau}_w - \tau_w}{\tau_w}$, where τ_w is the wall-shear stress obtained from DNS, and $\hat{\tau}_w$ is the value predicted by WMLES. Similar definitions for the heat flux error.

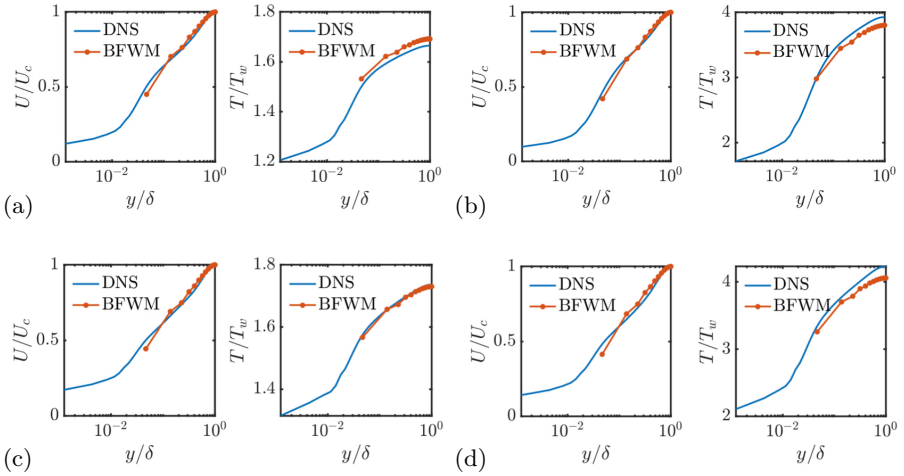

FIGURE 5. The mean velocity and mean temperature profiles of WMLES (red) using BFWM-rough wall model and DNS (blue solid) of a compressible channel flow over rough surface RS2 at (a) $M_c = 2, Re_c = 8000$, (b) $M_c = 4, Re_c = 8000$, (c) $M_c = 2, Re_c = 16000$, (d) $M_c = 4, Re_c = 16000$.

separate artificial neural networks: one for the shear stress model and another for the heat flux model. Each network follows a feedforward architecture with four hidden layers, each comprising 15 neurons, and is trained using gradient descent with momentum and an adaptive learning rate. To control overfitting, an L_2 regularization factor of 0.9 is employed. The data is partitioned into training, validation, and testing sets, with allocations of 70%, 15%, and 15%, respectively. The correlation between the predicted and actual values for both wall-shear stress and heat flux of the overall dataset exceeds 99%. Figure 3 displays the dimensionless wall- shear stress and heat flux as functions of the optimized dimensionless inputs, illustrating the continuous relationship predicted by the neural networks and providing a smooth approximation of the underlying data.

3. Results

3.1. *Compressible turbulent channel flow*

The performance of BFWM-rough is tested in compressible turbulent channel flows. The WMLES is driven with uniform volumetric forcing to achieve the same M_c and Re_c as

the corresponding DNS in Table 1, following Griffin *et al.* (2023). The cases are run on a domain with streamwise, wall-normal, and spanwise lengths of $(4\pi \times 2 \times \pi\sqrt{3})\delta$ and feature periodic boundary conditions in the streamwise and spanwise directions. The grid resolution is $dx = (\pi/16)\delta$, $dy = (1/24)\delta$, and $dz = (\sqrt{3}\pi/48)\delta$. The wall model matching location is the first control volume adjacent to the wall. For each Mach and Reynolds number, the WMLES is tested using 15 different rough surfaces, resulting in a total of 180 cases.

The *a-posteriori* error distribution of the BFWM-highspeed is shown in Figure 4. The mean *a-posteriori* relative errors for the wall-shear stress and heat flux are 11% and 12%, respectively. The mean velocity and temperature profiles for selected cases are shown in Figure 5.

3.2. *Turbulent compression ramp over a rough wall*

We assess the performance of BFWM-rough on a compression ramp with roughness at a hypersonic Mach number. The setup, shown in Figure 6(a), is similar to the experiments performed by Prince *et al.* (2005). The angle of the flap is 30°, the Mach number, based on the free-stream conditions, is $M_\infty = 8.2$, and the Reynolds number, based on the plate length L (defined as the distance from the leading edge to the start of the flap), and the free-stream conditions, is $Re = 1.44 \times 10^6$. In the experiment, roughness is introduced by covering the plate and flap with sandpaper, and the roughness in the simulations is modeled using the parameters $ES = 0.4$ and $k_{rms}/R_a = 1.24$. A uniform inflow is imposed at the inlet, a sponge zone is imposed at the outlet, and periodic boundary conditions are applied along the spanwise direction. The grid size in the farfield is constant and equal to $\Delta = 0.1L$. Close to the solid walls, the mesh is refined using 7 levels where the grid size for each level is reduced by 50%, leading to approximately 30 grids per boundary layer thickness at the hinge. A refinement window with a constant grid size of $\Delta \approx 30 \times 10^{-4} L$ is included over the plate to capture the shock wave that develops at the leading edge.

Figure 6(b) shows the evolution of the heat transfer coefficient, $C_H = \frac{q_w}{\rho_\infty U_\infty C p_\infty (T_w - T_r)}$, as a function of the streamwise position, where T_r is the recovery temperature. The results obtained with BFWM-rough are compared against the experimental measurements from Prince *et al.* (2005). The model accurately predicts the increase in heat flux at the flap, yielding good agreement with the experiments.

3.3. *EDL vehicle*

BFWM-rough is finally tested on a blunt-body entry vehicle. The WMLES corresponds to the experiment conducted at the NASA Langley Research Center 20-Inch Mach 6 Air Tunnel (Hollis 2014). The blunt-body model is a hemisphere with sand-grain roughness. The radius of the actual model is $R_B = 0.0762m$. BFWM-rough is validated against the roughness case '20-Mesh' in Hollis (2014) whose roughness height in viscous units, k^+, varies from 50 to 200 from the front center point to the trailing edge. The contour of temperature variation from the WMLES is shown in Figure 7(a). The freestream velocity, pressure, and temperature are set at the inflow boundary and domain boundaries in the y and z directions. A characteristic boundary condition with a damping function is applied in the volume near the outflow boundary (i.e., the sponge region) to minimize acoustic reflections from the computational outflow boundary. The Voronoi mesh is generated with a background grid size of $\Delta = 0.6R_B$. The grids near the hemisphere are refined by 10 levels where the grid size for each level is reduced by 50% to ensure about 6 control volumes resolve the boundary layer at the location $x/R_B = 0.4$, and a refinement window with 5 refined levels is applied at the shock wave locations.

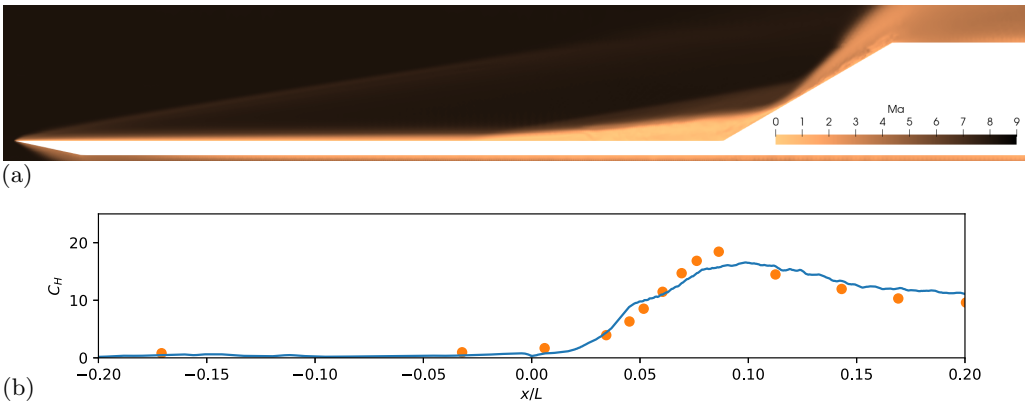

FIGURE 6. (a) Flow over the compression ramp. The magnitude shown is the instantaneous Mach number. (b) Heat transfer coefficient as a function of the streamwise direction. The origin corresponds to the start of the flap. Results obtained with WMLES BFWM-rough (solid line) are compared against experimental results from Prince *et al.* (2005) (dots).

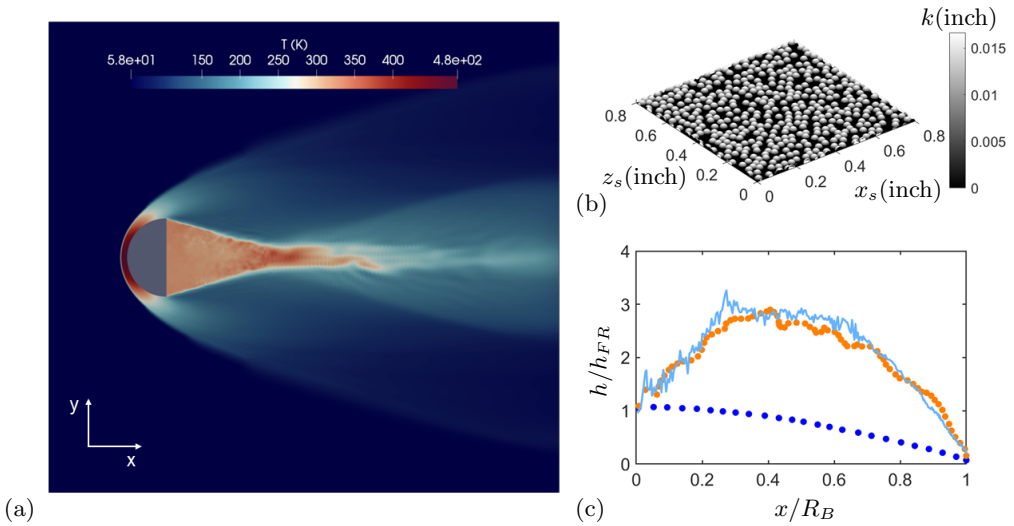

FIGURE 7. (a) Instantaneous flow field for WMLES of hemisphere with sand-grain distributed surface roughness at Mach 6 across a free stream Reynolds number $Re_\infty = 2.74 \times 10^7$/m. The contour shows the temperature variation at the plane $z = 0$. (b) A sample tile of the randomly distributed sand-grain roughness corresponding to the roughness case 20-Mesh in Hollis (2014). The contour shows the roughness elevation, and the unit is inch. (c) Heat distribution h/h_{FR} on the hemisphere, where h is the heat-transfer film coefficient, and h_{FR} is the heat-transfer film coefficient based on Fay-Riddell theory (Fay & Riddell 1958). The results of WMLES with BFWM-rough for 20-Mesh (line) are compared with the experimental results from Hollis (2014) for smooth (blue dots) and rough 20-Mesh (orange dots) surfaces.

The sand-grain roughness on the model is produced by applying an adhesive coating to a bed of manufactured, spherical glass particles. To extract the roughness parameters for BFWM-rough input, we generate a synthetic sand-grain roughness tile corresponding to the 20-Mesh roughness in Hollis (2014) by randomly distributing hemispherical elements on a flat surface. The resulting sample tile is shown in Figure 7(b). The roughness

parameters computed from the sample tile are $k_{rms}/Ra = 1.13$ and $ES = 0.53$. The time-averaged heat augmentation from WMLES with BFWM-rough is shown in Figure 7(c) and compared to the experimental results for a smooth surface and a rough 20-Mesh surface. For this problem, the flow over the hemisphere with a smooth surface remains laminar, whereas the roughness induces transition, and a turbulent boundary layer develops over the surface. For the case of 20-Mesh roughness, the boundary layer transition is induced by the roughness near the very front of the hemisphere. The heat augmentation distribution shows good agreement with the experiment from Hollis (2014).

4. Conclusions

We have developed a wall model for LES of high-speed flows. The model, referred to as BFWM-highspeed, is implemented via artificial neural networks that predict wall shear and heat flux over both smooth and rough surfaces. The model includes two components: BFWM-smooth and BFWM-rough. BFWM-smooth is trained using data from turbulent channel and pipe flows documented in the literature. BFWM-rough is trained with a new DNS database of high-speed turbulent channel flows over rough surfaces. An information-theoretic dimensional learning approach is employed to identify the most informative dimensionless inputs for predicting the nondimensionalized wall-shear stress and heat flux. The performance of BFWM-highspeed has been assessed *a-posteriori* in the WMLES of several validation cases, including turbulent channel flows, a compression ramp, and an EDL vehicle. Overall, 'BFWM-highspeed' offers predictions with a typical accuracy ranging from 1% to 12%. Future work will be devoted to improving the predictive capabilities of the model by expanding the training dataset and refining the SGS models.

Acknowledgments

This work was supported by the National Science Foundation under Award Number 2317254 and by an Early Career Faculty grant from NASA's Space Technology Research Grants Program (Grant Number 80NSSC23K1498). Y.L. was supported by The Boeing Company. The authors acknowledge the MIT SuperCloud and Lincoln Laboratory Supercomputing Center, as well as the Oak Ridge Leadership Computing Facility, which is a DOE Office of Science User Facility supported under Contract DE-AC05-00OR22725, for providing HPC resources that have contributed to the research results reported within this work.

REFERENCES

Arranz, G., Ling, Y., Costa, S., Goc, K. & Lozano-Durán, A. 2024 Building-block-flow computational model for large-eddy simulation of external aerodynamic applications. *Commun. Eng.* **3**, 127.

Bowersox, R. 2007 Survey of high-speed rough wall boundary layers: invited presentation. In *AIAA Paper 2007-3998*.

Coleman, G. N., Kim, J. & Moser, R. D. 1995 A numerical study of turbulent supersonic isothermal-wall channel flow. *J. Fluid Mech.* **305**, 159–183.

Cover, T. M. 1999 *Elements of Information Theory*. John Wiley & Sons.

Dirling, R. 1973 A method for computing roughwall heat transfer rates on reentry nosetips. In *AIAA Paper 1973-0763*.

Fay, J. A. & Riddell, F. R. 1958 Theory of stagnation point heat transfer in dissociated air. *J. Aerosp. Sci.* **25**, 73–85.

Finson, M. & Clarke, A. 1980 The effect of surface roughness character on turbulent re-entry heating. In *AIAA Paper 1980-1459*.

Fu, L., Karp, M., Bose, S. T., Moin, P. & Urzay, J. 2021 Shock-induced heating and transition to turbulence in a hypersonic boundary layer. *J. Fluid Mech.* **909**, A8.

Gaitonde, D. V. & Adler, M. C. 2023 Dynamics of three-dimensional shock-wave/boundary-layer interactions. *Annu. Rev. Fluid Mech.* **55**, 291–321.

Griffin, K. P., Fu, L. & Moin, P. 2023 Near-wall model for compressible turbulent boundary layers based on an inverse velocity transformation. *J. Fluid Mech.* **970**, A36.

Hansen, N., Müller, S. D. & Koumoutsakos, P. 2003 Reducing the time complexity of the derandomized evolution strategy with covariance matrix adaptation. *Evol. Comput.* **11**, 1–18.

Hollis, B. R. 2014 Distributed roughness effects on blunt-body transition and turbulent heating. In *AIAA Paper 2014-0238*.

Hollis, B. R., Berger, K. T., Berry, S. A., Brauckmann, G. J., Buck, G. M., DiFulvio, M., Horvath, T. J., Liechty, D. S., Merski, N. R., Murphy, K. J. *et al.* 2014 Entry, descent and landing aerothermodynamics: NASA Langley experimental capabilities and contributions. In *AIAA Paper 2014-1154*.

Iyer, P. S. & Malik, M. R. 2019 Analysis of the equilibrium wall model for high-speed turbulent flows. *Phys. Rev. Fluids* **4**, 074604.

Kawai, S. & Larsson, J. 2010 A dynamic wall model for large-eddy simulation of high reynolds number compressible flows. *Annual Research Briefs, Center for Turbulence Research, Stanford University,* pp. 25–37.

Lozano-Durán, A. & Bae, H. J. 2023 Machine learning building-block-flow wall model for large-eddy simulation. *J. Fluid Mech.* **963**, A35.

Ma, R., Alamé, K. & Mahesh, K. 2021 Direct numerical simulation of turbulent channel flow over random rough surfaces. *J. Fluid Mech.* **908**, A40.

Ma, R. & Lozano-Durán, A. 2024 Machine-learning wall-model large-eddy simulation accounting for isotropic roughness under local equilibrium. *arXiv Preprint arXiv:2406.00471* .

MacDonald, M., Chung, D., Hutchins, N., Chan, L., Ooi, A. & García-Mayoral, R. 2017 The minimal-span channel for rough-wall turbulent flows. *J. Fluid Mech.* **816**, 5–42.

Mettu, B. R. & Subbareddy, P. K. 2022 Wall-modeled large eddy simulation of high speed flows. *AIAA J.* **60**, 4302–4324.

Pérez-Ràfols, F. & Almqvist, A. 2019 Generating randomly rough surfaces with given height probability distribution and power spectrum. *Tribol. Int.* **131**, 591–604.

Prince, S. A., Vannahme, M. & Stollery, J. L. 2005 Experiments on the hypersonic turbulent shock-wave/boundary-layer interaction and the effects of surface roughness. *Aeronaut. J.* **109**, 177–184.

Vreman, A. W. 2004 An eddy-viscosity subgrid-scale model for turbulent shear flow: Algebraic theory and applications. *Phys. Fluids* **16**, 3670–3681.

Yang, X., Urzay, J., Bose, S. & Moin, P. 2018 Aerodynamic heating in wall-modeled large-eddy simulation of high-speed flows. *AIAA J.* **56**, 731–742.